Role of the near-tip region of a fin in fish propulsion

F. J. Huera-Huarte[1] and Morteza Gharib[2]
[1]*Department of Mechanical Engineering, Universitat Rovira i Virgili (URV), 43007 Tarragona, Spain*
[2]*Division of Engineering and Applied Science, California Institute of Technology, Pasadena, California 91125, USA*

(Received 17 January 2019; published 17 June 2019)

Fish combine a wide variety of passive and active control mechanisms to generate thrust. Muscle actuation is used by fish in order to dynamically alter the shape or the stiffness of different parts of the body, to ultimately control propulsion. We uncover the effects of locally altering the tip region of a flapping fin system, by using a low-order robotic model. We show how the actuation of this region can largely modify propulsion. Detailed forces and torque measurements and a low-order eigenmode reconstruction of the flow around the flapping fin show the effects of varying the phase difference between the tip region and the body of the fin on the propulsive performance. Kinematics that force the trailing edge to move behind the main body of the fin are beneficial in terms of efficiency and thrust generation. For a very small range of phase differences, large thrusts can be combined with large side forces that could be used by fish to increase maneuverability.

DOI: 10.1103/PhysRevFluids.4.063103

I. INTRODUCTION

Compliance is a widespread characteristic associated with the locomotion of aquatic animals across scales. It is also well known that fish combine this passive characteristic with a wide variety of active control mechanisms to actuate their propulsive appendages to generate thrust [1]. Several authors [2,3] have hypothesized that muscle control is used by fish in order to control stiffness of different parts of the body, to ultimately control propulsion. This implies that fish not only can actively change the shape of their appendages, but also can stiffen them to allow more or less deformation. Precise timings of muscle activation in the body of sharks while swimming have been described and found to be synchronized with the fish midline curvature and, therefore, with tail beating [4,5]. Fish *et al.* [6] showed how a phase difference of $\pi/2$ between the fin and the peduncle region in dolphins was beneficial for propulsion. Other authors [7,8] have shown how, when using heaving/pitching mechanisms to simulate fish propulsion, that phase seems to be optimal. Actuation of a specific set of muscles has been observed using electromyography [9] during steady swimming. Although it seems obvious that fish alter the mechanical characteristics of their fins while swimming, results showing this behavior locally at the fin have barely been reported. Flammang [10] studied the function of the radialis muscle, in the upper lobe of the caudal fin of a shark, when changes in swimming conditions were imposed. The radialis has been recognized as a specialized muscle used to change the structural characteristics of the fin.

The use of simplified models based on panels, plates, and foils undergoing pitch and/or heave motions is extended as a way to fundamentally study aquatic locomotion. When the flexibility of the fins is taken into account in these simplified models, it is usually assumed to be constant and passive, with values of the order of those measured in fish [11] and at comparable Reynolds numbers, in the range of 10^3 to 10^6, depending on the species [12,13]. The effects of stiffness on the forces and efficiency produced by flapping flexible foils have been studied in works such as those by Prempraneerach *et al.* [14], Fish and Lauder [15], Lauder and Madden [16], Alben [17], Lucas *et al.* [18],

Heathcote *et al.* [19], Feilich and Lauder [20], and Huera-Huarte [21], among others. These have helped us to better understand the flow-structure interactions that lead to the propulsion of the fish. Lauder *et al.* [22] concluded that active capabilities should be added to simplified robotic models to reach a better understanding of locomotion in fish and recognized it as a key challenge in propulsion studies. Attempts have been made by the same groups using more advanced robotic models [23–25] to study the effects of active control strategies directed at producing changes in the shape of the fins, mimicking fin-ray actuation.

Using a passive pitching panel with different planforms and stiffnesses, Park *et al.* [26] investigated compliance effects on fish propulsion. The authors centered their study on the analysis of the phase delay between the trailing edge of their system and the main pitching motion of the foil. They showed that when the phase was near $\pi/2$, with the trailing edge lagging the main rotation shaft, propulsion was maximized and concluded that, independently of the shape, for a flexible fin to be optimal at different operating frequencies, stiffness should be actively modified. This is a consequence of the very complex nonlinear interplay between the stiffness of the fin and the fluid. If fish had appendages characterized by a uniform constant and fixed stiffness, they could only be efficient at a certain Reynolds number, the one that would produce the specific deflection that leads to efficient propulsion under that condition. Conversely, their ability to control their propulsive appendages in many ways allows them to adjust to many different conditions. Therefore, in order to study in an overall manner the effects of flexibility, a system that allows changes in the deflections of the foil when flapping (or indirectly the stiffness) is needed. A system such as the one presented here, which allowsdifferent kinematics during the flapping cycle, is well suited for that purpose.

In their 2016 study Park *et al.* [27] provided more physical insight into the $\pi/2$ delay condition observed in their previous study. In a recent study, Huera-Huarte [21] described in detail the impulse generated by foils of different stiffnesses. The study of the time series of thrust force in conjunction with a synchronized analysis of the vortex structures in the near-wake allowed the identification of the physical causes for the different performances observed. The author used qualitative estimations of the momentum transfer to the wake to explain the different impulsive behaviours observed. The concept was based on the idea that in viscous flows, vorticity can be considered to be confined in a thin vortex loop of circulation (Γ), hence the force generated by a panel rotating in a fluid can be linked to the time rate of change of the circulation and the size of the vortex formed [28,29],

$$\mathbf{F}(t) = -\rho \frac{d}{dt}(\Gamma \mathbf{S}), \tag{1}$$

where $\mathbf{S}$ is the area enclosed by the vortex loop in the wake. Considering a two-dimensional wake modeled by point vortices [30], the forcing can be related to the time rate of change of circulation and the separation of the vortex dipole (Δy) formed at each side of the propulsor,

$$F_i \cong -\rho \frac{d}{dt} \sum_i \Gamma_i \Delta y_i. \tag{2}$$

The same approach was used by Huera-Huarte and Gharib [31] in experiments conducted with a foil having fixed deformations near its trailing edge. Both studies were limited to the analysis of impulsive motions of either flexible foils or rigid foils that had different curvatures near the trailing edge. It was found that foils whose tip region was inclined to the suction side when rotating showed larger impulsive performance compared to straight foils, as the inclination imposed a delay in the tip vortex formation that resulted in an enhanced vortex structure in the near-wake. At the same time, the work suggested that the same inclination at the very last part of the stroke was beneficial because it diverted the flow that travels parallel to the fin towards the tip, ending up better aligned with the thrust direction. Therefore, considering periodic flapping events, at the end of the stroke, when the second half of the flapping cycle is starting, the slope should be changed immediately. Two conditions, with in-phase and out-of-phase motions of the tip, were then studied, evidencing the possibilities of dynamic tip actuation. The study, however, was limited to the case of single-stroke kinematics of the foils. Hence, the need for a detailed study of the case of an active trailing edge in

periodic flapping and the implications of the phase difference in the motion, as in the work presented here, was evident. The experimental system used for this work allows not only periodic motions but also the measurement of other mechanical quantities needed to compute efficiencies, which could not be implemented with the previous setup.

For the work presented here, we designed a simplified robotic model that allows us to control the pitch position of the tip region of a rectangular fin, independently of the pitch imposed on the whole system. The model was inspired by the ability of certain species to locally produce alterations in curvature using muscle actuation, as discussed in the previous paragraphs. The fin is, in fact, a low-order model of a fish appendage especially designed to avoid the need to deal with the flexibility as a variable. It is based on pure pitching and, therefore, inspired by fish that propel themselves by moving the last part of their body such as Carangiform, Thunniform, and Ostraciiform swimmers [12], although the experiment is designed to enhance our physical understanding of flapping propulsion in general, not considering particular species. Two clear regions can be identified, the main body and the tip region near the trailing edge. We uncover the effects of changing dynamically the relative position of both regions, i.e., the curvature at the very last part of the rigid fin. The phase difference between the motions of these two regions emerges as a crucial parameter for understanding propulsion. By modifying this phase difference we can simulate a wide variety of situations, from those in which the tip is not actuated as in a completely rigid fin to cases in which the trailing edge moves behind or ahead of the fin. This system overcomes the limitations of passive flapping systems for the study of fish propulsion, as pointed out by many authors previously [22,26,27].

II. METHODS

A. A robotic fin with an active trailing edge

The robotic fin is based on two rigid three-dimensional printed parts made of polylactic acid. The main body of the fin is rectangular, with a span (s) of 200 mm, a chord (c_f) of 95 mm, and a thickness of 12 mm. It is controlled by means of a servo that actuates a 6-mm shaft (main shaft) embedded in the body of the fin. The second part is the tip or the trailing edge, with the same span, a chord (c_t) of 20 mm, and a thickness of 12 mm that decreases smoothly to the trailing edge. The overall chord (c) of the fin is 120 mm, leading to an aspect ratio (s/c) of 1.7. The body of the fin has two shafts (secondary and tip shafts) each rotating around several miniature bearings and connected by a timing belt. The secondary shaft is controlled by another smaller servo, so when it rotates, it produces identical rotations in the tip shaft and therefore in the trailing-edge part. This belt configuration was used to avoid having the tip servo directly coupled to the tip shaft, protruding around that area and modifying the flow around the fin. The same fin design was used in the work by Huera-Huarte and Gharib [31], but here several new sensors have been added to the system as in the work by Huera-Huarte [32]. The main shaft is geared to a precision potentiometer (300° range with an accuracy of 2%), so its angular position is measured at all times and the imposed kinematics can be verified. In order to measure the torques applied to the main shaft during the operation of the robotic fin, a torque sensor characterized by a measurement range of ± 5 N m, with an accuracy of $\pm 0.2\%$ of its full scale range, has been used. Details of the apparatus are illustrated in Fig. 1.

An in-house-developed code uploaded to dedicated electronics allowed the independent control of each servo. The servos were powered by a laboratory power supply at 6 V (able to deliver up to 0.7 N m), and controlled by two pulse-width-modulated signals. The software permitted the control of the amplitude and the frequency of each servo shaft rotation independently, therefore the phase difference between the rotations of each one could be controlled too.

B. Experimental setup

The robotic system was installed vertically, on top of a water tank of dimensions $1 \times 1.1 \times 2.25$ m as depicted in the lateral schematic in Fig. 2. It was installed hanging from a six-axis load

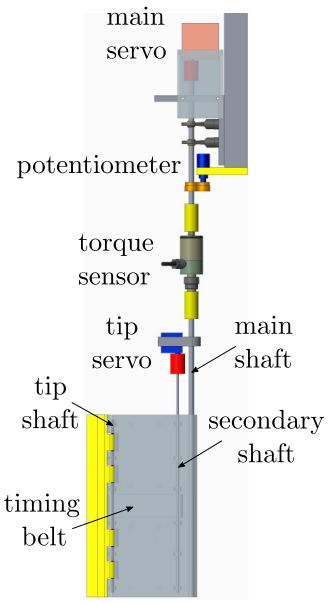

FIG. 1. Lateral schematic of the robotic fin used for the experiments.

cell with a measurement range of 100 N for forces and 10 N m for moments, by means of several specially designed parts. The load cell was attached to an air-bearing carriage that was restricted to movement along a rectangular beam with a cross section of 50.8×50.8 mm^2 and a local straightness accuracy of 25 μm/m over its entire length. When pressurized air, at more than 6 bar, was supplied to the carriage, it could move with no friction along the rectangular beam. Its motion was restricted, however, by a uniaxial precision load cell with a measurement range of ± 8.9 N that was connected to the air-bearing carriage and to an external structure by means of universal joints, preventing the appearance of reaction moments on it. The thrust force measurements were conducted with the two load cells (the six-axis and the uniaxial one) redundantly, with both signals showing extremely good agreement, with differences of less than 3%. A detailed comparison of the forces using these two methods, in a similar setup but in an experiment involving fluid-structure interactions of a a cylinder, is given by Huera-Huarte [33].

A Cartesian coordinate system has been defined with its origin at the midspan point of the fin, with z along the main shaft and the x aligned with the direction of the thrust force imposed by the air-bearing rig. The fin was installed centered in the water tank, so the free surface and the bottom and lateral walls were always far enough away to avoid any interference. Experiments were conducted in quiescent fluid, i.e., without free stream velocity, in order to avoid the formation of leading-edge vortices at the rotating shaft of the flapping system, which are known to interact with trailing-edge ones depending on the current characteristics and, therefore, posing added complexity to the problem not desired at this stage, as in other works such as the study by Van Buren *et al.* [34].

All signals, including the main shaft rotation, the main shaft torque, and the output of the multiaxis and the uniaxial load cells, were synchronously sampled at 2 kHz using a dedicated data acquisition system controlled by an in-house code developed for the experiments. Data were low pass filtered at 35 Hz (all physics were of the order of 1 Hz or multiples) using a zero-phase distortion digital filter, to remove unwanted 50-Hz noise signals coming from the building electrical supply. A digital particle image velocimetry (DPIV) system [35] was installed in the tank in order to visualize the flow structures generated by the flapping device. The water tank was seeded with 10-μm polystyrene fluorescent spheres and a Nd:YAG pulsed green laser source was used to illuminate the tracer particles. The laser was installed on one of the sides of the tank and a planar

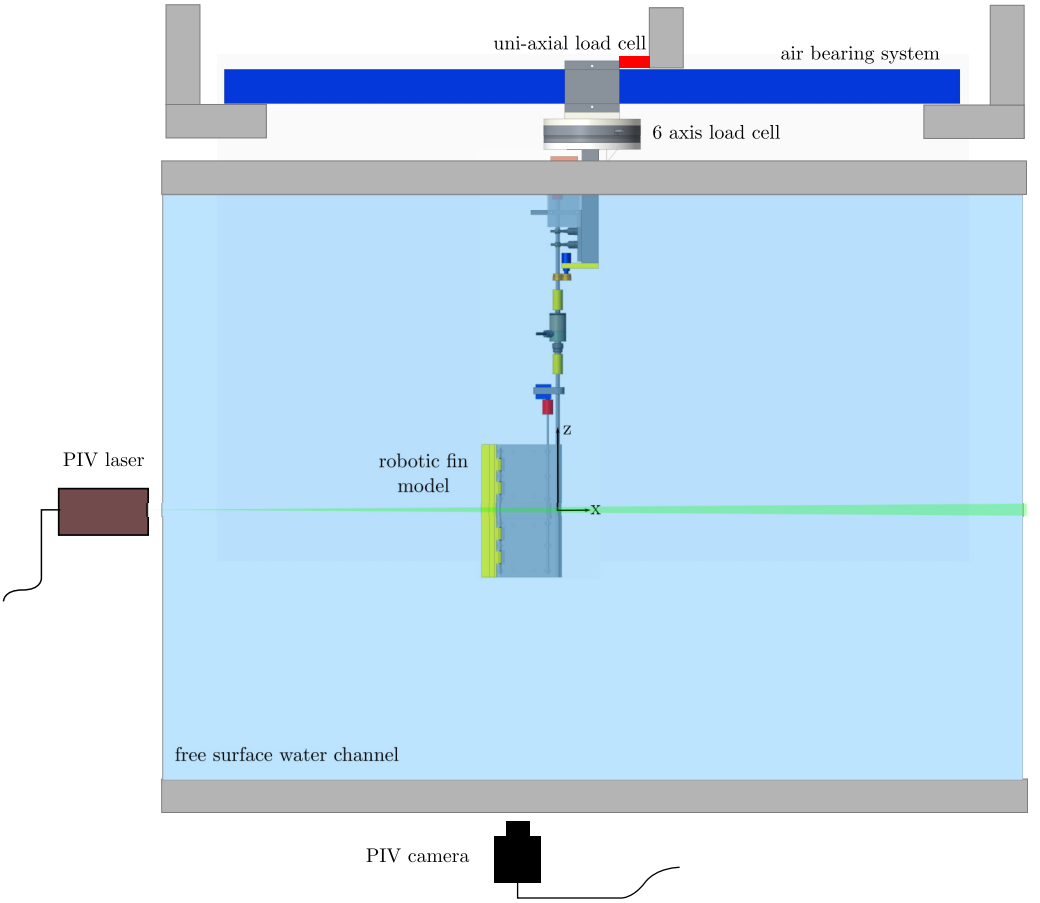

FIG. 2. Lateral schematic view of the experimental setup. The robotic fin appears hanging from a six-axis load cell installed in an air-bearing system. A uniaxial load cell is used to have redundant measurements of the thrust forces generated by the system.

xy sheet was generated aiming at the midspan of the fin. Using a combination of front surface mirrors and adequate optics, shadows were minimized around the fin. An in-house-written code allowed control of the laser and synchronization of the illumination pulses with a digital camera. The camera was based on a monochrome 12-bit, 2-megapixel CCD sensor, fitted with a 24-mm fixed-focal-length objective. The system was configured to acquire a pair of full-resolution images every 76.9 ms (13 Hz), with a spacing between images in the pair (Δt) of 4 ms. A lateral schematic view of the setup is shown in Fig. 2.

C. Kinematics imposed on the fin

The pulse-width-modulated signals that were used to control the servos were programmed to impose sinusoidal motions to the main and secondary shafts. The sinusoidal rotations in the shaft of the servos resulted in independent pitch motions of the fin and the tip, with kinematics that can be described by the equations

$$\theta_f(t) = \theta_{f_0} \sin(\omega_f t), \quad \theta_t(t) = \theta_{t_0} \sin(\omega_t t + \phi), \tag{3}$$

where θ_{f_0} is the amplitude of the pitch angle imposed on the main body of the fin through the main servo, and θ_{t_0} is the amplitude of the pitch angle at the tip by means of the secondary servo.

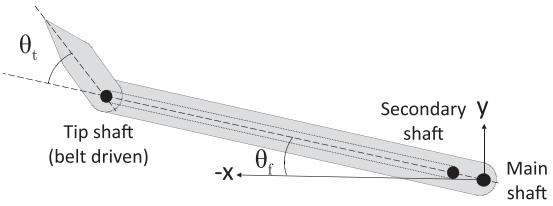

FIG. 3. Schematic of the robotic fin including the definition of the main kinematic variables.

$\omega_f = 2\pi f_f$ and $\omega_t = 2\pi f_t$ are the circular frequencies imposed on the system. Details of the angles presented in the equations appear in the schematic in Fig. 3.

Even though the amplitudes and frequencies in the equations could be controlled independently, for all cases presented in this work, they were kept constant, with values of $\theta_0 = \theta_{f_0} = \theta_{t_0} = 30^\circ$ and $f = f_f = f_t = 2/3$ Hz, respectively. The effects of amplitude and angular velocity or frequency were thoroughly studied in a previous work [31] and they are kept constant here in order to reduce the very large parameter space associated with the kinematics of the robotic fin. The study focus here is on the effects of the phase difference between the two motions ϕ, which was systematically varied in steps of 15° during the experiments, covering all possible phase difference situations to mimic nature's ability to locally and dynamically stiffen or alter the shape of propulsive appendages. Experiments without trailing-edge control were also carried out in order to have the rigid fin as the reference case. In such cases the trailing edge was permanently aligned with the main body of the fin. For the sake of clarity, details of the kinematics for four selected cases, with $\phi = -180^\circ$ (out of phase), $\phi = -90^\circ$, $\phi = 0^\circ$ (in phase), and $\phi = 90^\circ$, are illustrated in Fig. 4. For each phase condition, the fin is shown at four positions in a cycle, with the first two being for the first half of the flapping cycle rotating in the clockwise direction and the last two for the second half of the cycle.

III. RESULTS AND DISCUSSION

A. Dimensionless parameters

The time derivatives in Eq. (4) provide the angular velocities of the system. We consider the angular velocity of the main body,

$$\Omega(t) = \dot{\theta_f}(t) = \omega\theta_0 \cos(\omega t) = \Omega_0 \cos(\omega t), \tag{4}$$

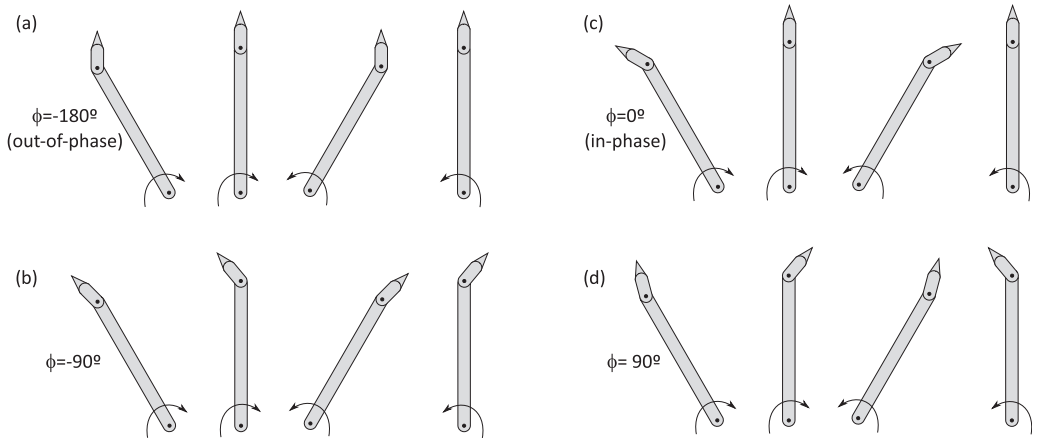

FIG. 4. Schematic of the kinematics of the robotic fin flapping in four phase difference configurations: (a) for $\phi = -180^\circ$ (out of phase), (b) for $\phi = -90^\circ$, (c) for $\phi = 0^\circ$ (in phase), and (d) for $\phi = 90^\circ$

and therefore the velocity of the tip for the case of the rigid fin is

$$V(t) = \Omega_0 c \cos(\omega t) = V_0 \cos(\omega t), \tag{5}$$

and we consider the average velocity of the trailing or tip of the fin $\overline{V} = \overline{\Omega} c$, therefore the Reynolds number becomes

$$\mathrm{Re} = \frac{\overline{V} c}{\nu} = \frac{\overline{\Omega} c^2}{\nu}, \tag{6}$$

with ν being the kinematic viscosity of the fluid. The average velocity derives from the total swept angle in a cycle and the oscillation period imposed. Because the kinematics are fixed in the main shaft, the Re is constant in the experiments, with a value of approximately 13 000, representative of fish swimming as noted in Sec. I [12,13]. Hydrodynamic force coefficients result from the time series of the thrust force (F_x), side force (F_y), and torque (M_z):

$$C_T = \frac{F_x}{\frac{1}{2}\rho \overline{V}^2 A}, \tag{7}$$

$$C_S = \frac{F_y}{\frac{1}{2}\rho \overline{V}^2 A}, \tag{8}$$

$$C_M = \frac{M_z}{\frac{1}{2}\rho \overline{V}^2 A s}. \tag{9}$$

The power coefficient is computed using the time series of the mechanical power in the main shaft. The power in the secondary shaft was not measured, as it was impossible to install a torque sensor without perturbing locally the flow in such a small shaft. Moreover, the measurement would be contaminated by the frictions of the components such as the belt and shaft supports packed inside the limited space of the body of the fin. In any case, the mechanical power associated with the torque in the secondary shaft is expected to be negligible compared to the power in the main shaft, because although the moving part at the trailing edge is one-sixth of the total chord, the effective change in the chord total length due to tip actuation is of the order of 1%, compared to the rigid case, because of the small angle involved in the motion:

$$C_P = \frac{M_z \Omega}{\frac{1}{2}\rho \overline{V}^3 A}. \tag{10}$$

In the equations, ρ is the fluid density and A the fin reference area (cs). In the following sections, mean values of the thrust ($\overline{C}_T$) and power ($\overline{C}_P$) coefficients, as well as standard deviations of the side force ($\widetilde{C}_S$) and torque coefficients ($\widetilde{C}_M$), are reported. We consider as well the efficiency of the system, defined as

$$\eta = \frac{\overline{C}_T}{\overline{C}_P}, \tag{11}$$

as well as the ratio of thrust to side force,

$$\zeta = \frac{\overline{C}_T}{\widetilde{C}_S}. \tag{12}$$

B. Role of the phase difference in flapping forces and efficiencies

Figure 5 shows the thrust, side force, and torque coefficients as a function of the imposed phase difference between the main body of the fin and the trailing edge. In all three plots, the dashed horizontal line is used to indicate the values obtained with the rigid fin, i.e., with the trailing part not moving. Each point in the plots is the result of an experiment that consisted of more than 15 flapping

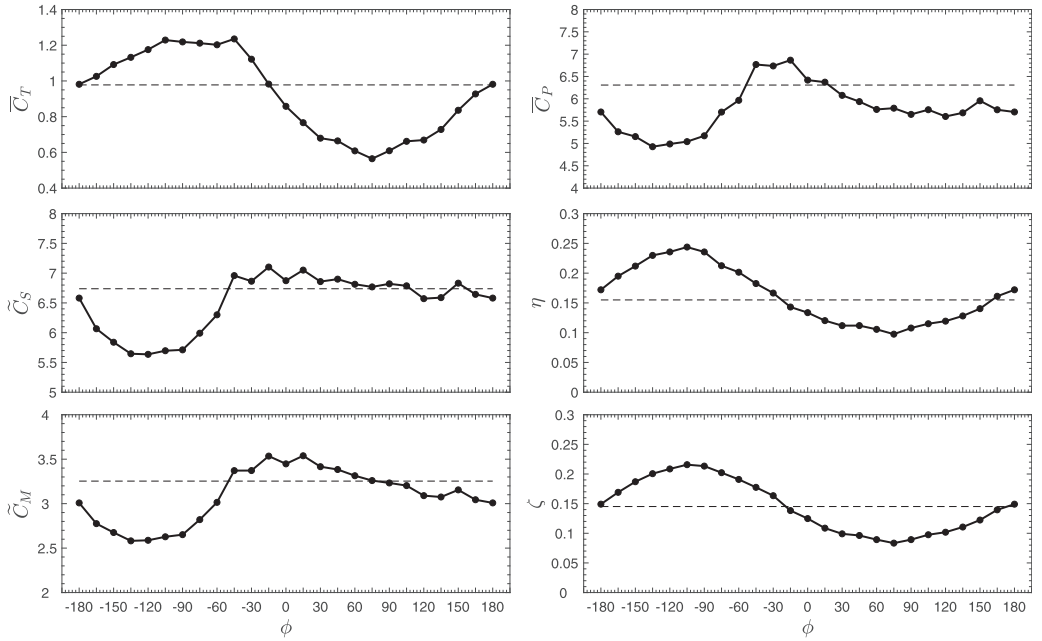

FIG. 5. Mean thrust coefficient (C_T), standard deviation of the side force (C_S), main shaft torque (C_M), mean power coefficient (C_P), efficiency (η), and ratio of thrust to side force (ζ) as a function of the phase difference imposed between the main body of the fin and the tip. The dashed horizontal line in all plots is used to indicate the results obtained with the reference rigid case.

cycles. The thrust force is larger than that produced by the rigid fin when the tip moves behind (lags) the main body of the fin, i.e., for the experiments conducted with $\phi < -15^\circ$. In the range -180° to -105° the thrust increases monotonically with the phase difference up to its maximum value near 1.2, which occur in the range -105° to -45°. With phase differences larger than -45° the thrust starts to decrease rapidly. With a 0° phase difference, the thrust is already 15% smaller than that of the rigid fin, and it continues decreasing to its minimum value, near 0.55, which is 45% smaller than with the rigid fin, found for a phase difference near 75°. It is clear from the experiments that when the trailing edge moves ahead of the main body of the fin, which occurs for all positive phase differences, the thrust is minimized. The trends exhibited by the side force and the main shaft torque differ considerably from that of the thrust force. They both are minimized in the range -180° to -60°, depicting a convex shape that reaches a value near 5.5 for the side force and 2.5 for the torque coefficient. Both coefficients are larger than that of the rigid fin only in the range -60° to 90°. They become smaller again for $\phi > 90^\circ$.

The power coefficient presented in the upper plot in Fig. 5 shows a trend similar to that of the side force and torque coefficients. It decreases from the out-of-phase configuration to the -90° phase condition and then it starts increasing up to its maximum value of 7, reached in the range -30° to 0°. If the phase difference is increased further, the power decreases slowly and then stays at values near 5.5 in the range 60° to 180°. Except for phases in the range -30° to 30°, the power is smaller than that of the rigid fin as indicated by the dashed horizontal line. The efficiency of the system η evolves in a sinusoidal manner with the phase difference as imposed by the thrust coefficient. In the out-of-phase condition it has a value similar to the one observed with the rigid fin, at about 13%, and as the phase difference grows it starts to increase up to its maximum, achieved at approximately -105° with an efficiency of 25%, to continue decreasing to the levels of the rigid fin under the in-phase condition, again on par with the rigid fin. For positive phase differences efficiencies are

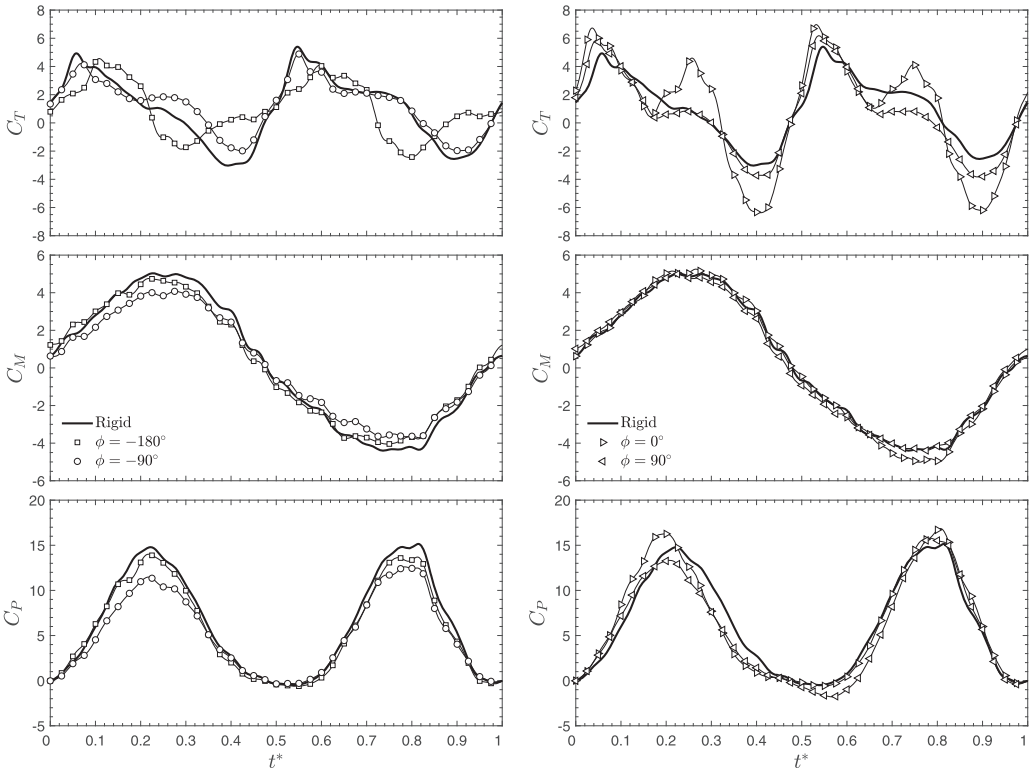

FIG. 6. Time-averaged cycles for the thrust, side force, and power for the rigid case and for cases with phase differences of $-180°$, $-90°$, $0°$, and $90°$. Time is in dimensionless form $t^* = tf$.

smaller than those of the rigid fin, with a local minimum slightly less than 10%. The ratio of thrust to side force follows a very similar trend with the phase difference, with values that oscillate from a minimum at around 10% to a maximum near 22%.

Detailed analysis of the time series of the force signals allows a better understanding of the phenomena observed. Cycle-averaged time series of the thrust, torque, and power coefficients are reported in Fig. 6 for cases with phase differences of $-180°$ and $-90°$ and cases with phase differences of $0°$ and $90°$, as a function of the dimensionless time $t^* = tf$. The difference between the measured values in all cycles was found to be extremely low, of the order of $\approx$1%, indicating the high cyclic repeatability achieved. It is also noteworthy how similar the signals measured during both halves of the cycle are, as it is common in other works [26,27] to have asymmetries that the authors attribute to intrinsic uncertainties in the drive mechanisms or small, yet very difficult to avoid, deviations in the geometry of the foils, which are not present here. The experiments in the figures are all cases that showed very different behavior in the previous phase difference plots. At $t^* = 0$ the fin is in one of the extreme positions of the cycle, and at $t^* = 0.5$ it is on the other side of the flapping cycle. In all plots the time series of the coefficients for the rigid fin are also included (solid black line) for reference. The two main positive peaks that appear per cycle, especially clear in the rigid fin case, are due to added mass effects in each one of the two strokes per cycle. As the thrust starts to decrease after the peak to the minimum values, it goes through a plateau (or secondary peak). These secondary intermediate positive peaks or plateaus have a circulatory origin and are caused by the shedding of the tip vortices during the motion of the fin [31]. In summary, in each cycle there is a large positive peak in thrust as the fin accelerates the fluid surrounding the system ($t^* \approx 0.05$ and $t^* \approx 0.55$), and just after that, the thrust starts to

decrease until the tip vortices are shed ($t^* \approx 0.25$ and $t^* \approx 0.75$), the time at which the thrust stops decreasing, remaining on a plateau or forming a smaller secondary positive peak. Negative thrust peaks follow, at dimensionless times $t^* \approx 0.4$ and $t^* \approx 0.9$. A detailed physical explanation of these forcing events was provided by Huera-Huarte [21] and Huera-Huarte and Gharib [31], based on a topological analysis of the near-wake [see Eq. (2)], which ultimately allowed qualitative estimations of the momentum transfer to the wake and therefore of the reacting impulse. In these two works it was shown how the chordwise flexibility and localized static deflections at the trailing edge altered the time at which tip vortices were shed and how they changed the shape of the thrust curves, in the starting-flow single-stroke maneuvers performed. Here, with periodic motions imposed on the fin, it is obvious from the time series in the figures that different phase differences ϕ modify the shape of the thrust curves as well.

In the upper plot in Fig. 6, the rigid fin shows the first peaks at approximately $t^* \approx 0.05$ and 0.55 and the two smaller circulatory events at $t^* \approx 0.25$ and 0.75, while in the case of a phase difference of -180° and -90° the events are not only modified in magnitude but also delayed. The maximum instantaneous thrust achieved in both cases is smaller than the one produced by the rigid fin, but the negative peaks are smaller as well, resulting in higher overall mean thrusts, as shown in Fig. 5. Torque coefficients are slightly smaller in the cases with a negative phase difference compared to the rigid fin, with something similar occurring with the side forces, not shown for the sake of brevity. In the lower plot it is shown that power coefficients are reduced compared to those in the rigid fin case.

If the phase difference is configured to be positive as in the two representative cases in Fig. 6, the main peaks appear earlier ($t^* \approx 0.02$ and $t^* \approx 0.52$) in time compared to the reference rigid case. The secondary peaks or plateaus take place at similar times. In the case with a phase difference of 0°, the magnitude of the secondary peak is very large, comparable to the main peak in the rigid case. Notwithstanding that the magnitude of the instantaneous thrust is larger than in the rigid cases, due to the fact that the negative peaks are also larger, the mean thrusts achieved end up being smaller as shown in Fig. 5. It is remarkable how in the case with $\phi = 0^\circ$, the intermediate peaks due to tip vortex shedding are especially high, due to an increased absolute tip velocity, even though the velocities in the main body of the fin are the same in all cases. The case of the torque coefficients (and the side forces, not shown for brevity) shows all lines collapsed, indicating practically no influence of the phase difference. The power shown in the lower plot in the figure has instantaneous values that are in general on par with those of the rigid fin and the ones presented in Fig. 6 for the negative phase difference cases.

In general, there are large differences in the thrust signals but not in the torque and the power signals. This indicates that the considerable changes reported in the efficiency of the system are mostly due to the differences in thrust and not in the power input to the system. The time series of the power needed to produce the motion of the system barely changes, but the amount of the total force produced in the x direction is heavily modified by the active tip. Figure 7 shows a vector representation of the total forces acting on the fin, in the form of a total force coefficient vector ($\vec{C}_F$) computed using the same nondimensionalization as in Eq. (7) but using the magnitude of the thrust and side forces. In the upper part of the plot the two thick lines represent the envelope of the motion of the fin for reference, without showing the tip region. The plot clearly shows that the phase angle controls the angle at which the force is oriented, reinforcing the information presented in Fig. 6.

C. Wake dynamics using the proper orthogonal decomposition (POD)

The analysis of the flow dynamics around the flapping fin gives more insight to explain the underlying causes of the variations observed in the performance of the system. In recent work by the authors [21,31], specific events in the time series of the forces were linked to the flow dynamics in the wake. Although efficiencies were not available because the torque was not measured, the DPIV measurements conducted in quiescent fluid in single-stroke motions allowed precise tracking of the evolution of the vortex formation processes, which were in turn related to the impulsive forces.

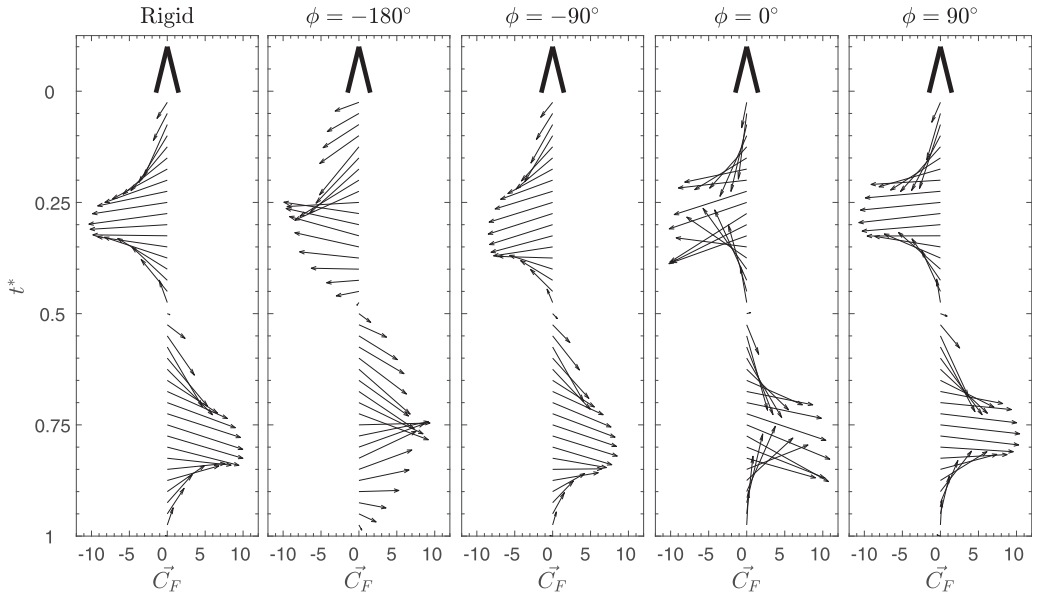

FIG. 7. Time evolution of the total force coefficient $\vec{C}_F$ for the cases presented in Fig. 6.

Here, motions are periodic, implying more complexity in the flow field in the near-wake, with the flow being perturbed cycle after cycle. We limit the discussion here to the spatiotemporal-averaged magnitude of the velocity fields around the fin. These are analyzed for the case of the rigid fin and for two more cases with phase differences of $-90°$ and $90°$ (best and worst performance).

Figures 8(a)–8(c) show the dimensionless form of the averaged velocity fields in the thrust direction ($\overline{u}/\overline{V}$), i.e., along x. The flow fields presented in the figure are a low-order representation of the DPIV data obtained during the experiments and were obtained using the three most energetic flow eigenmodes after a POD of the experimental results. In all the plots the position of the robotic fin is indicated in the extremum positions for clarity (the trailing edge is presented without showing its actual deflection for simplicity as in Fig. 7). The POD can be seen as a filter that removes structures in the flow associated with a very low kinetic energy or not coherent in time and space. In this case with periodic flapping and very complex flow in the near-wake of the system, this yields a better representation of the data without losing any generality; see more details in the Appendix and in the work by Huera-Huarte and Vernet [36].

The first POD mode ψ^1, i.e., the most energetic, of the in-line velocity component, for each of the three experiments, appears in Figs. 8(d)–8(f), depicting a clear similitude in terms of structure with the averaged flow fields in Figs. 8(a)–8(c). This implies that most of the kinetic energy injected into the fluid during the flapping motions results in velocity in the thrust direction. The case associated with the best performance, for a phase difference of $-90°$, exhibits the largest area with high x velocities in the left column in Fig. 8, especially compared to the $90°$ phase case. The differences, however, are smaller compared to the rigid fin case, when simply looking at the average flow fields. When examining the energy content associated with the POD modes in each of the three cases, differences are clear and intensified, as shown in the POD spectrum in Fig. 9. The figure depicts the energy associated with the first eight POD modes for the rigid fin case and for the cases analyzed in Fig. 8, with phase differences of $-90°$ and $90°$, the best and worst performance, respectively. In all cases, the energy of the first mode (ϵ_1) is the largest, with the first POD mode (ψ^1) coping with approximately one-third of the total energy in the wake, depending on ϕ. Interestingly, the highest kinetic energy in the thrust direction among all the cases is that of the case that showed the highest performance in terms of thrust and efficiency, i.e., the one corresponding to a phase

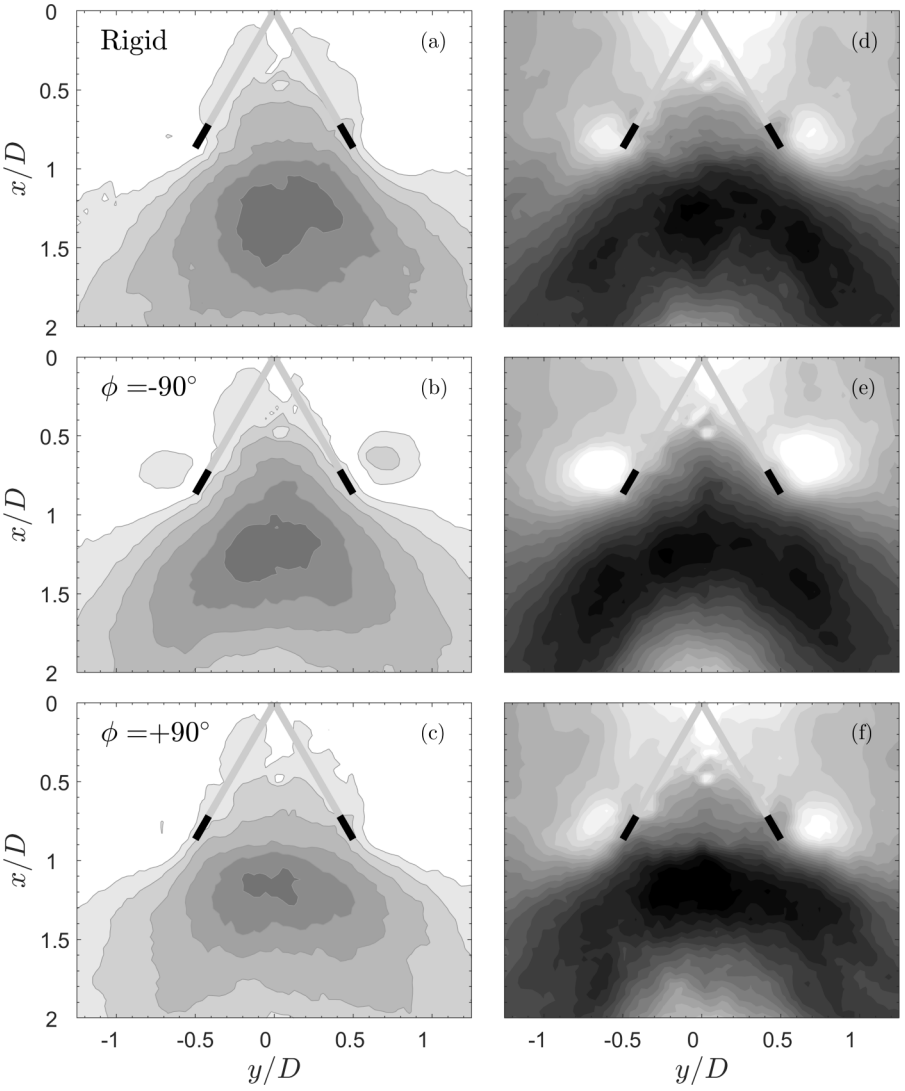

FIG. 8. (a)–(c) Magnitude of the mean in line with the flow velocity field ($\overline{u}/\overline{V}$) for the rigid case and for two cases with -90° and 90° phase differences. (d)–(f) First POD mode (ψ^1) of the in-line velocity for the same cases.

difference $\phi = -90^\circ$. It has been shown in the previous section that C_T was largely modified with changes in ϕ, and now we can see how from the flow perspective, the energy associated with the first POD mode in the thrust direction directly correlates with the performance exhibited. The higher the kinetic energy of the first POD mode in the thrust direction, the higher the performance observed in the experiment. The amount of momentum transferred to the wake in the x direction is the largest in cases where the thrust is the highest because the force appears as a reaction to the rate of change of the momentum. An estimation of the importance of this momentum transferred to the wake in the direction of the thrust can be obtained by computing the time-averaged momentum flux coefficient

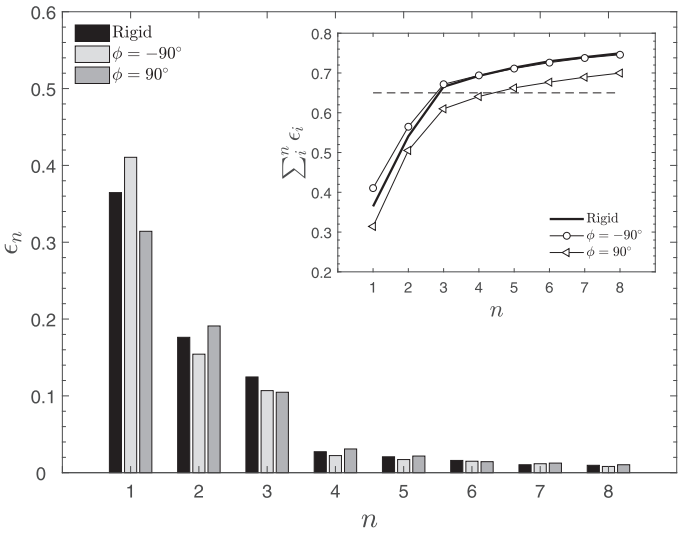

FIG. 9. POD modal kinetic energy (ϵ_n) spectra for all phase differences investigated. Inset: The kinetic energy in cumulative form.

in the x direction,

$$\overline{C_{f_x}} = \frac{1}{\frac{1}{2}\overline{V}^2 l_y c} \int_{y_1}^{y_2} \overline{u}^2(x_i, y) dy, \tag{13}$$

integrated from $y_1 = -1.5D$ to $y_2 = +1.5D$, with l_y being the distance between y_1 and y_2, and at a certain x_i in the near-wake (around the tip region). Results for x_i in the range from 0 to 1.25 are reported in the lower plot in Fig. 10. It is shown that the $\overline{C_{f_x}}$ values are the largest for the case with $\phi = -90°$, again justifying the enhanced thrust indicated by the POD analysis. The two upper plots in the figure represent the $\rho\overline{u}^2$ distributions along the y direction, at two x locations near the tip of the flapping system. These curves present clear differences between the three configurations investigated.

D. Implications for swimmers and discussion

Phase differences with negative values have been shown to result in increased thrusts and efficiencies. These cases have imposed kinematics that lead to curvatures in the same directions as systems with a fixed flexibility deforming passively. In cruising situations a fish would configure its fins in order to generate the highest thrust and the minimal side force, reducing the need for lateral stabilization mechanisms yielding the highest efficiency. We have observed that such performance takes place within our system when phases are configured in the range $-105° < \phi < -45°$. A constant-stiffness appendage would always result in a fixed curvature or deformation for a given tail beat, while one with the ability to modify the stiffness would be able to produce changes equivalent to the phase differences in our system, leading to precise changes in the performance as seen in the experiments. Moreover, in the narrow range $-45° < \phi < -15°$, the system delivers a high thrust with a high side force that could be used for increased maneuverability. The largest sidewise maneuverability is observed with positive phases in the range $0° < \phi < 90°$, with large side forces and minimal thrust.

On the other hand, compliance has been associated in the past with increased performances compared to rigid propulsors. In this sense, the work presented here, showing cases with the trailing edge moving behind the fin as in a passive configuration, also supports the idea that compliance in

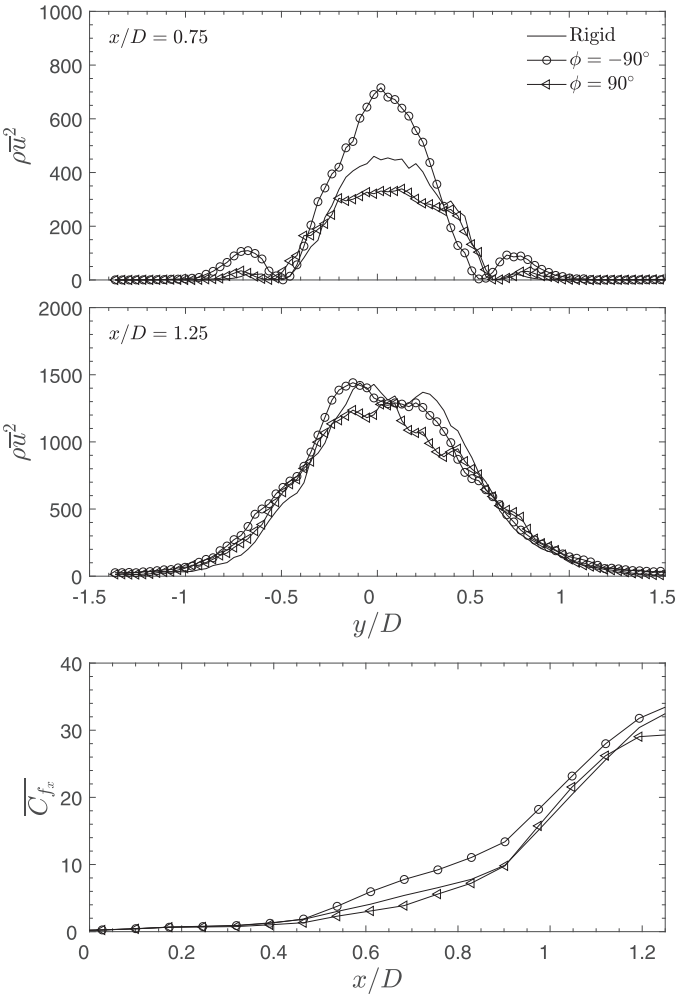

FIG. 10. Momentum flux coefficient C_{f_x} as a function of x in the region near the tip of the flapping system. Distributions of $\rho\overline{u}^2$ along the y direction, at $x/D = 0.75$ and $x/D = 1.25$.

a propulsive appendage results in enhanced performance. However, in general most authors have studied the effects of flexibility using foils or systems with a constant stiffness, hence with fixed passively given kinematics, where the deformations or curvatures are also fixed by the fluid-structure coupling. It has been pointed out in previous work [22,26,27] that the study of systems with active capabilities is crucial if the purpose is to better understand propulsive phenomena in nature. The results presented here clearly indicate that a dynamic variation of the very last part of our robotic fin produces profound changes in the overall propulsive behavior of the system. Moreover, we have been able to investigate cases that would not naturally develop in passive systems, which has allowed us to further understand the role of a phase difference inside the appendage itself. When a fish alters the stiffness of a specific part of its fin, it indirectly does the same with the deformation and the curvature of the fin, and that is known to produce changes in thrust [10]. We have shown here that although the control strategies used by living organisms are of extreme complexity, as they imply different types of tissue and cartilaginous and bony structures, similar effects can be triggered by actively changing locally the shape (curvature) of a reduced-order system such as the one presented here. Moreover, the fact that the fin developed for this work has only two degrees of freedom is

also especially interesting when considering the implementation of these strategies in underwater propulsion systems.

IV. CONCLUDING REMARKS

A low-order model of a fish fin has been implemented in a simplified robotic device, based on two moving parts independently controlled. The system has allowed us to show how a phase difference between the tip region and the fin itself leads to large modifications in thrust and efficiency. This mechanism of local actuation, which has been observed in real fish before, has never been studied with a low-order model such as the one presented here. The system allows us to simulate a wide variety of scenarios not explored before with a simplified model, ranging from those with kinematics similar to those typical of passive flexibility to others possible only if forced motions are imposed.

The work demonstrates how the local control of a fin can largely modify propulsion. In nature, this is thought to be a common mechanism to control momentum transfer to the wake and therefore hydrodynamic forces. Kinematics that force the trailing edge to move behind the main body of the fin are beneficial in terms of efficiency and thrust generation. In a very small range of phase differences, large thrusts can be combined with large side forces to increase maneuverability. A POD-based flow decomposition has shown that the energy associated with the most energetic mode in the flow, which indicates high velocities in the thrust direction, is altered by changing the kinematics of the fin.

ACKNOWLEDGMENTS

The authors would like to acknowledge the funding provided by the Spanish Ministerio de Economía y Competitividad through Grant No. DPI2015-71645-P and the Gordon and Betty Moore Foundation through Grant No. GBMF4038 to the California Institute of Technology.

APPENDIX: PROPER ORTHOGONAL DECOMPOSITION

The POD, principal component analysis, or Karhunen-Loéve transform [37] is used to decompose velocity fields and other spatiotemporal fields into spatial POD modes or basis functions ($\psi(x, y)$) and time-dependent modal coefficients ($a(t)$). The fluctuating part of the flow can be computed as linear combinations of POD modes $\psi_i(x, y)$ and time-varying modal coefficients $a_i(t)$,

$$U(x, y, t) = \bar{U}(x, y) + \sum_{i=1}^{M} a_i(t)\psi_i(x, y). \tag{A1}$$

In Sec. III C the snapshot POD method is applied to the DPIV data obtained during some of the experiments. The velocity field can be organized instantaneously, i.e., at each time instant (t^n), in a column vector ($\tilde{\mathbf{u}}^n$), with the first lm elements being the x or in-line velocity (u_i) and the last lm the y or transverse velocity (v_i):

$$\tilde{\mathbf{u}}^n = [u_1(t^n) \dots u_{lm}(t^n) v_1(t^n) \dots . v_{lm}(t^n)]^T. \tag{A2}$$

Bold symbols indicate vector quantities. Hence, having N snapshots, the velocity field of an experiment can be expressed using a $2lm \times N$ matrix in which each column is a vector field (snapshot) and each row gives the two components of the velocity vector at the different locations:

$$\tilde{\mathbf{U}} = [\tilde{\mathbf{u}}^1 \cdots \tilde{\mathbf{u}}^N]. \tag{A3}$$

Moreover, the fluctuating part of the flow can be computed as

$$\mathbf{U} = \tilde{\mathbf{U}} - \bar{\mathbf{u}} = \tilde{\mathbf{U}} - \frac{1}{N}\sum_{n=1}^{N} \mathbf{u}^n, \quad n = 1, 2, \dots, N. \tag{A4}$$

The eigenvalue problem derived from the application of the snapshot POD method is given by the equation

$$\mathbf{C}\mathbf{H}^i = \lambda^i \mathbf{H}^i, \tag{A5}$$

where the matrix $\mathbf{C}$ is [38]

$$\mathbf{C} = \mathbf{U}^T\mathbf{U}. \tag{A6}$$

The solution of Eq. (A5) consists of N eigenvalues (λ^i) and the $N \times N$ modal matrix ($\mathbf{H}$), made of column eigenvectors ($\mathbf{H}^n$). The eigenvectors provide a basis to produce the POD modes,

$$\phi^i = \frac{\sum_{n=1}^{N} H_n^i \mathbf{u}^n}{\left|\left| \sum_{n=1}^{N} H_n^i \mathbf{u}^n \right|\right|}, \quad i = 1, 2, \ldots, N, \tag{A7}$$

where $||\cdot||$ denotes the *p2* norm, and it is calculated as the square root of the summation of the squares of each component within the brackets. The result of Eq. (A7) is a set of N POD modes of dimension $2lm$. Retrieving Eq. (A1), the flow can be expressed as a linear combination of POD modes and POD coefficients,

$$\mathbf{u}^n = \sum_{n=1}^{N} a_i^n \psi^i = \mathbf{\Psi}\mathbf{a}^n; \tag{A8}$$

hence, once the POD modes are available, the POD coefficients ($\mathbf{a}^n$) can be obtained,

$$\mathbf{a}^n = \mathbf{\Psi}^T\mathbf{u}^n. \tag{A9}$$

These coefficients indicate how important each POD mode is in each time snapshot. The eigenvalues (λ^i) are proportional to the kinetic energy of the fluctuating part of the flow, and by sorting them in a decreasing fashion, $\lambda^i > \lambda^{i+1}$ for $i = 1, \ldots, N-1$, the most energetically important POD modes in the flow can be identified. The relative kinetic energy associated with each POD mode can be calculated as

$$\varepsilon_i = \frac{\lambda^i}{\sum_{n=1}^{N} \lambda^n}. \tag{A10}$$

With the time-dependent POD coefficients and the POD eigenmodes available, Eqs. (A1) and (A8) allow a low-order reconstruction of the fluctuating velocity field at any instant in time ($\mathbf{u}^n$):

$$\mathbf{u}^n = \bar{\mathbf{u}} + \sum_{i=1}^{M} a_i^n \psi^i = \bar{\mathbf{u}} + \mathbf{\Psi}\mathbf{a}^n. \tag{A11}$$

[1] R. Bainbridge, Caudal fin and body movement in the propulsion of some fish, J. Exp. Biol. **40**, 23 (1963).
[2] R. McN. Alexander, The lift produced by the heterocercal tails of Selachii, J. Exp. Biol. **43**, 131 (1965).
[3] J. H. Long and K. S. Nipper, The importance of body stiffness in undulatory propulsion, Integr. Comp. Biol. **36**, 678 (1996).
[4] J. M. Donley, Steady swimming muscle dynamics in the leopard shark Triakis semifasciata, J. Exp. Biol. **206**, 1117 (2003).
[5] J. M. Donley, Patterns of red muscle strain/activation and body kinematics during steady swimming in a lamnid shark, the shortfin mako (Isurus oxyrinchus), J. Exp. Biol. **208**, 2377 (2005).
[6] F. E. Fish, J. E. Peacock, and J. J. Rohr, Stabilization mechanism in swimming odontocete cetaceans by phased movements, Mar. Mammal Sci. **19**, 515 (2003).

[7] J. M. Anderson, K. Streitlien, D. S. Barrett, and M. S. Triantafyllou, Oscillating foils of high propulsive efficiency, J. Fluid Mech. **360**, 41 (1998).
[8] D. A. Read, F. S. Hover, and M. S. Triantafyllou, Forces on oscillating foils for propulsion and maneuvering, J. Fluids Struct. **17**, 163 (2003).
[9] B. E. Flammang and G. V. Lauder, Speed-dependent intrinsic caudal fin muscle recruitment during steady swimming in bluegill sunfish, Lepomis macrochirus, J. Exp. Biol. **211**, 587 (2008).
[10] B. E. Flammang, Functional morphology of the radialis muscle in shark tails, J. Morphol. **271**, 340 (2010).
[11] M. McHenry, C. Pell, and J. H. Long Jr., Mechanical control of swimming speed: Stiffness and axial wave form in undulating fish models, J. Exp. Biol. **198**, 2293 (1995).
[12] M. Sfakiotakis, D. M. Lane, and J. B. C. Davies, Review of fish swimming modes for aquatic locomotion IEEE J. Ocean. Eng. **24**, 237 (1999).
[13] M. Gazzola, M. Argentina, and L. Mahadevan, Scaling macroscopic aquatic locomotion, Nat. Phys. **10**, 758 (2014).
[14] P. Prempraneerach, F. S. Hover, and M. S. Triantafyllou, The effect of chordwise flexibility on the thrust and efficiency of a flapping foil, International Symposium on Unmanned Untethered Submersible Technology (2003).
[15] F. E. Fish and G. V. Lauder, Passive and active flow control by swimming fishes and mammals, Annu. Rev. Fluid Mech. **38**, 193 (2006).
[16] G. V. Lauder and P. G. A. Madden, Fish locomotion: Kinematics and hydrodynamics of flexible foil-like fins, Exp. Fluids **43**, 641 (2007).
[17] S. Alben, Optimal flexibility of a flapping appendage in an inviscid fluid, J. Fluid Mech. **614**, 355 (2008).
[18] K. N. Lucas, N. Johnson, W. T. Beaulieu, E. Cathcart, G. Tirrell, S. P. Colin, B. J. Gemmell, J. O. Dabiri, and J. H. Costello, Bending rules for animal propulsion.Nat. Commun. **5**, 3293 (2014).
[19] S. Heathcote, Z. Wang, and I. Gursul, Effect of spanwise flexibility on flapping wing propulsion, J. Fluids Struct. **24**, 183 (2008).
[20] K. L. Feilich and G. V. Lauder, Passive mechanical models of fish caudal fins: Effects of shape and stiffness on self-propulsion, Bioinspirat. Biomimet. **10**, 036002 (2015).
[21] F. J. Huera-Huarte, On the impulse produced by chordwise flexible pitching foils in a quiescent fluid, J. Fluids Eng. **140**, 1 (2018).
[22] G. V. Lauder, B. Flammang, and S. Alben, Passive robotic models of propulsion by the bodies and caudal fins of fish, Integr. Comp. Biol. **52**, 576 (2012).
[23] C. Phelan, J. Tangorra, G. Lauder, and M. Hale, A biorobotic model of the sunfish pectoral fin for investigations of fin sensorimotor control, Bioinspirat. Biomimet. **5**, 035003 (2010).
[24] J. Tangorra, C. Phelan, C. Esposito, and G. Lauder, Use of biorobotic models of highly deformable fins for studying the mechanics and control of fin forces in fishes, Integr. Comp. Biol. **51**, 176 (2011).
[25] C. J. Esposito, J. L. Tangorra, B. E. Flammang, and G. V. Lauder, A robotic fish caudal fin: Effects of stiffness and motor program on locomotor performance, J. Exp. Biol. **215**, 56 (2012).
[26] Y. J. Park, U. Jeong, J. Lee, S. R. Kwon, H. Y. Kim, and K. J. Cho, Kinematic condition for maximizing the thrust of a robotic fish using a compliant caudal fin, IEEE Trans. Robot. **28**, 1216 (2012).
[27] H. Park, Y. J. Park, B. Lee, K. J. Cho, and H. Choi, Vortical structures around a flexible oscillating panel for maximum thrust in a quiescent fluid, J. Fluids Struct. **67**, 241 (2016).
[28] J. C. Wu, Theory for aerodynamic force and moment in viscous flows, AIAA J. **19**, 432 (1981).
[29] P. G. Saffman, *Vortex Dynamics* (Cambridge University Press, Cambridge, UK, 1992).
[30] B. Protas and J. E. Wesfreid, On the relation between the global modes and the spectra of drag and lift in periodic wake flows, C.R. Mécanique **331**, 49 (2003).
[31] F. J. Huera-Huarte and M. Gharib, On the effects of tip deflection in flapping propulsion, J. Fluids Struct. **71**, 217 (2017).
[32] F. J. Huera-Huarte, Propulsive performance of a pair of pitching foils in staggered configurations, J. Fluids Struct. **81**, 1 (2018).
[33] F. J. Huera-Huarte, Dynamics and excitation in a low mass-damping cylinder in cross-flow with side-by-side interference, J. Fluid Mech. **850**, 370 (2018).

[34] T. Van Buren, D. Floryan, N. Wei, and A. J. Smits, Flow speed has little impact on propulsive characteristics of oscillating foils, Phys. Rev. Fluids **3**, 1 (2018).
[35] C. E. E. Willert and M. Gharib, Digital particle image velocimetry, Exp. Fluids **10**, 181 (1991).
[36] F. J. Huera-Huarte and A. Vernet, Vortex modes in the wake of an oscillating long flexible cylinder combining POD and fuzzy clustering, Exp. Fluids **48**, 999 (2010).
[37] J. L. Lumley, The structure of inhomogeneous turbulent flows, in *In Atmospheric Turbulence and Radio Wave Propagation*, edited by A. M. Yaglom and V. I. Tatarski (Nauka, Moscow, 1967), pp. 166–178.
[38] L. Sirovich, Proper orthogonal decomposition applied to turbulent flow in a square duct, Q. Appl. Math. **45**, 561 (1987).